

# Morphology and density structure of post-CME current sheets

B. Vršnak<sup>1</sup>, G. Poletto<sup>2</sup>, E. Vujčić<sup>3</sup>, A. Vourlidas<sup>4</sup>, Y.-K. Ko<sup>4</sup>, J. C. Raymond<sup>5</sup>, A. Ciaravella<sup>6</sup>, T. Žić<sup>1</sup>, D. F. Webb<sup>7</sup>, A. Bemporad<sup>8</sup>, F. Landini<sup>9</sup>, G. Schettino<sup>9</sup>, C. Jacobs<sup>10</sup>, and S. T. Suess<sup>11</sup>

<sup>1</sup> Hvar Observatory, Faculty of Geodesy, Zagreb, Croatia

<sup>2</sup> INAF-Arcetri Observatory, Firenze, Italy

<sup>3</sup> Faculty of Science, Geophysical Department, Croatia

<sup>4</sup> Naval Research Laboratory, Washington DC, USA

<sup>5</sup> Harvard-Smithsonian Center for Astrophysics, Cambridge, USA

<sup>6</sup> INAF-Palermo Observatory, Palermo, Italy

<sup>7</sup> Boston College and AFRL, Hanscom, USA

<sup>8</sup> INAF-Torino Astrophysical Observatory, Pino Torinese, Italy

<sup>9</sup> Dept. of Astronomy and Space Science, University of Florence, Italy

<sup>10</sup> Centrum voor Plasma-Astrofysica, K. U. Leuven, Belgium

<sup>11</sup> NASA Marshall Space Flight Center, Huntsville, USA

Received 22 August 2008 / Accepted 6 February 2009

## ABSTRACT

**Context.** Eruption of a coronal mass ejection (CME) drags and “opens” the coronal magnetic field, presumably leading to the formation of a large-scale current sheet and the field relaxation by magnetic reconnection.

**Aims.** We analyze physical characteristics of ray-like coronal features formed in the aftermath of CMEs, to check if the interpretation of this phenomenon in terms of reconnecting current sheet is consistent with the observations.

**Methods.** The study is focused on measurements of the ray width, density excess, and coronal velocity field as a function of the radial distance.

**Results.** The morphology of rays indicates that they occur as a consequence of Petschek-like reconnection in the large scale current sheet formed in the wake of CME. The hypothesis is supported by the flow pattern, often showing outflows along the ray, and sometimes also inflows into the ray. The inferred inflow velocities range from 3 to 30 km s<sup>-1</sup>, consistent with the narrow opening-angle of rays, adding up to a few degrees. The density of rays is an order of magnitude larger than in the ambient corona. The density-excess measurements are compared with the results of the analytical model in which the Petschek-like reconnection geometry is applied to the vertical current sheet, taking into account the decrease of the external coronal density and magnetic field with height.

**Conclusions.** The model results are consistent with the observations, revealing that the

Report Documentation Page				Form Approved OMB No. 0704-0188	
Public reporting burden for the collection of information is estimated to average 1 hour per response, including the time for reviewing instructions, searching existing data sources, gathering and maintaining the data needed, and completing and reviewing the collection of information. Send comments regarding this burden estimate or any other aspect of this collection of information, including suggestions for reducing this burden, to Washington Headquarters Services, Directorate for Information Operations and Reports, 1215 Jefferson Davis Highway, Suite 1204, Arlington VA 22202-4302. Respondents should be aware that notwithstanding any other provision of law, no person shall be subject to a penalty for failing to comply with a collection of information if it does not display a currently valid OMB control number.					
1. REPORT DATE <b>26 JUN 2010</b>		2. REPORT TYPE		3. DATES COVERED <b>00-00-2010 to 00-00-2010</b>	
4. TITLE AND SUBTITLE <b>Morphology and density structure of post-CME current sheets</b>				5a. CONTRACT NUMBER	
				5b. GRANT NUMBER	
				5c. PROGRAM ELEMENT NUMBER	
6. AUTHOR(S)				5d. PROJECT NUMBER	
				5e. TASK NUMBER	
				5f. WORK UNIT NUMBER	
7. PERFORMING ORGANIZATION NAME(S) AND ADDRESS(ES) <b>Hvar Observatory,,Faculty of Geodes,Zagreb, Croatia, ,</b>				8. PERFORMING ORGANIZATION REPORT NUMBER	
9. SPONSORING/MONITORING AGENCY NAME(S) AND ADDRESS(ES)				10. SPONSOR/MONITOR'S ACRONYM(S)	
				11. SPONSOR/MONITOR'S REPORT NUMBER(S)	
12. DISTRIBUTION/AVAILABILITY STATEMENT <b>Approved for public release; distribution unlimited</b>					
13. SUPPLEMENTARY NOTES					
14. ABSTRACT <b>Eruption of a coronal mass ejection (CME) drags and ?opens? the coronal magnetic field, presumably leading to the formation of a large-scale current sheet and the field relaxation by magnetic reconnection. Aims. We analyze physical characteristics of ray-like coronal features formed in the aftermath of CMEs, to check if the interpretation of this phenomenon in terms of reconnecting current sheet is consistent with the observations. Methods. The study is focused on measurements of the ray width, density excess, and coronal velocity field as a function of the radial distance. Results. The morphology of rays indicates that they occur as a consequence of Petschek- like reconnection in the large scale current sheet formed in the wake of CME. The hypothesis is supported by the flow pattern, often showing outflows along the ray and sometimes also inflows into the ray. The inferred inflow velocities range from 3 to 30 kms&amp;#8722;1, consistent with the narrow opening-angle of rays, adding up to a few degrees. The density of rays is an order of magnitude larger than in the ambient corona. The density-excess measurements are compared with the results of the analytical model in which the Petschek-like reconnection geometry is applied to the vertical current sheet taking into account the decrease of the external coronal density and magnetic field with height.</b>					
15. SUBJECT TERMS					
16. SECURITY CLASSIFICATION OF:			17. LIMITATION OF ABSTRACT <b>Same as Report (SAR)</b>	18. NUMBER OF PAGES <b>23</b>	19a. NAME OF RESPONSIBLE PERSON
a. REPORT <b>unclassified</b>	b. ABSTRACT <b>unclassified</b>	c. THIS PAGE <b>unclassified</b>			

main cause of the density excess in rays is a transport of the dense plasma from lower to larger heights by the reconnection outflow.

**Key words.** Sun: coronal mass ejections (CMEs) – Sun: corona – (Sun:) solar wind – magnetohydrodynamics (MHD)

## 1. Introduction

According to the current comprehension of solar coronal mass ejections (CMEs), the eruption of an unstable magnetic structure is tightly associated with the formation of the large scale current sheet (hereinafter CS) in the wake of the eruption. This concept, connecting the large scale eruption and the localized energy release in a form of flare, was put forward and initially developed by Carmichael 1964; Sturrock 1966; Hirayama 1974; Kopp & Pneuman 1976 (the so-called CSHKP model). When the current sheet becomes long enough, the tearing instability sets in, leading to fast reconnection of magnetic field (for the analytical, numerical, laboratory, and observational results see, e.g., Furth et al. 1963; Ugai 1987; Gekelman & Pfister 1988; Vršnak et al. 2003, respectively). Reconnection in the post-CME current sheet results in an abrupt energy release causing a flare, and on the other hand, enhances and prolongs the acceleration of the erupting magnetic field structure (e.g., Lin 2004; Vršnak 2008, and references therein). Numerical MHD simulations covering various scales, from low corona up to 1 AU, also demonstrated post-CME current sheet formation, clearly revealing the importance of the reconnection in the initiation, acceleration, and propagation of CMEs (see, e.g., Riley et al. 2002; Roussev et al. 2003; Török et al. 2004; Riley et al. 2007, for a review see Forbes et al. 2006).

The most prominent consequence of CME-associated reconnection is the appearance of the so called two-ribbon flare, closely synchronized with the CME acceleration stage (e.g., Maričić et al. 2007, and references therein). The ribbon expansion away from the magnetic inversion line, associated with growing system of hot loops connecting the ribbons, has led to the formulation of the CSHKP model. The discovery of cusped structure above the flare loops (e.g., Tsuneta et al. 1992; Forbes & Acton 1996; Tsuneta 1996), looptop hard X-ray sources (e.g., Masuda et al. 1994; Aschwanden et al. 1996; Sui et al. 2004; Veronig et al. 2006), the loop shrinkage (e.g., Švestka et al. 1987; Forbes & Acton 1996; Sheeley et al. 2004; Vršnak et al. 2006), and the recognition of growing posteruption loop systems in the absence of flares, further supported the CSHKP scenario. Additional evidence for reconnection below the erupting flux-rope may be found in the so-called disconnection events (e.g., Webb & Cliver 1995; Simnett et al. 1997; Wang et al. 1999), downflows above the post-eruption arcades (e.g., McKenzie & Hudson 1999; Innes et al. 2003; Asai et al. 2004), horizontal converging flows above the loops (Yokoyama et al. 2001; Lin et al. 2005), and flare-associated radio emission below the eruptive prominence (Vršnak et al. 2003).

Recently, post-CME features seen in UV spectra (Ciaravella et al. 2002; Ko et al. 2003; Innes et al. 2003b; Lin et al. 2005; Bemporad et al. 2006; Ciaravella & Raymond 2008), X-ray images (Sui et al. 2004, 2005), and white light coronagraph images (Ko et al. 2003; Webb et al. 2003; Lin et al. 2005) have been attributed to the current sheets expected to

“connect” the flare loops to the CME core. The UV spectral signature is generally emission in the high temperature lines of Fe XVIII or Fe XIX formed at 5–10 MK. EUV images from the Extreme-ultraviolet Imaging Telescope (EIT) on board the Solar and Heliospheric Observatory (SoHO) and the Transition Region and Coronal Explorer (TRACE) show emission in Fe XXIV at even higher temperatures (McKenzie & Hudson 1999; Innes et al. 2003). The UV features decay slowly, on time scales from several hours (Ciaravella & Raymond 2008) up to a few days (Bemporad et al. 2006; Ko et al. 2003). The X-ray data from the Reuven Ramaty High Energy Solar Spectroscopic Imager (RHESSI) show regions of high temperature emission above loop tops, and both the morphology at different energies and the evolution of the structures supports the CS identification. The white light features are bright, narrow rays that appear to map from the cusped flaring loop system to the CME core (Lin et al. 2005). Some show blobs of plasma moving outwards at several hundred  $\text{km s}^{-1}$ . Like the UV features, the white light structures can last for a day or two. In general, white light observations reveal the electron column density, UV data show temperatures, emission measures and Doppler shifts, and X-ray observations reveal very high temperature plasma.

The aim of this paper is to demonstrate that post-CME rays appear as a consequence of the reconnection in the current sheet formed in the wake of CME, and to quantify their basic physical characteristics. We outline the working hypothesis in Sect. 2, whereas details of the model used to compare the theoretical expectations with observations are provided in the Appendix. Observations and measurements are presented in Sect. 3, focusing on the morphology and plasma densities in post-CME rays. The temperature structure and the ionization state will be presented in a separate paper. Our density measurements are compared with the model estimates and some previous empirical results in Sect. 4. Results are discussed and conclusions drawn in Sect. 5.

## 2. Working hypothesis

Since post-CME rays extend outward from cusped structures associated with growing post-eruption loop-systems, our working hypothesis is that they appear as a consequence of the reconnection in the CS formed in the wake of CME. Furthermore, we assume the reconnection process can be approximately described in terms of the steady-state Petschek regime (Petschek 1964). In this regime, the reconnection takes place within a small diffusion region (DR), out of which two pairs of standing slow-mode shocks (SMSs) extend along of the axis of symmetry. Thus, the CS is bifurcated, with SMSs separating the inflow and outflow region (Petschek 1964; Soward & Priest 1982). At SMSs the inflowing plasma is compressed, heated, and accelerated, forming the upward and downward reconnection jet (Fig. 1). Note that electric currents are concentrated only in DR and SMSs.

When reconnection takes place in the homogeneous environment, the characteristics of outflowing plasma are determined primarily by the external plasma-to-magnetic pressure ratio, whereas the outflow speed is approximately equal to the external Alfvén speed (see Appendix in Aurass et al. 2002; Skender et al. 2003). However, in the case of a vertical current sheet, the ambient coronal density and magnetic field decrease with height, so

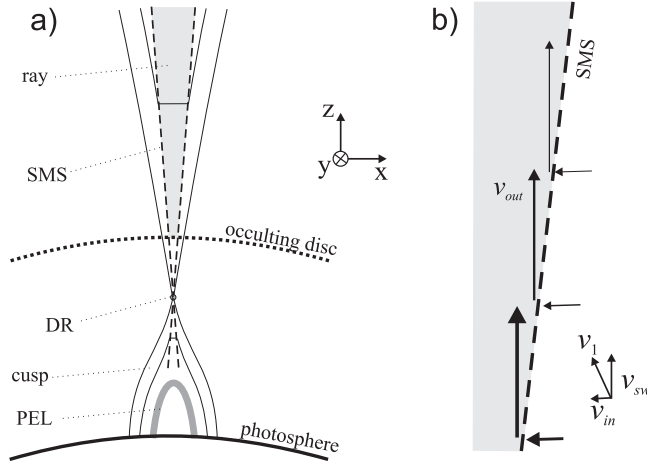


**Fig. 1.** a) Interpretation of the ray in terms of the Petschek (1964) reconnection model: DR – diffusion region; SMS – slow mode shocks (dashed lines intersecting at DR); PEL – post-eruption loops. Magnetic field-lines are drawn by thin lines; gray area between the SMSs outlines the post-CME ray. The coordinate system is indicated (the line of sight is in  $y$ -direction). b) An element of bifurcated current sheet; arrows mark plasma flows ( $v_{in}$  – inflow velocity;  $v_{sw}$  – solar wind speed;  $v_{out}$  – outflow speed), where the arrow thickness depicts plasma densities.

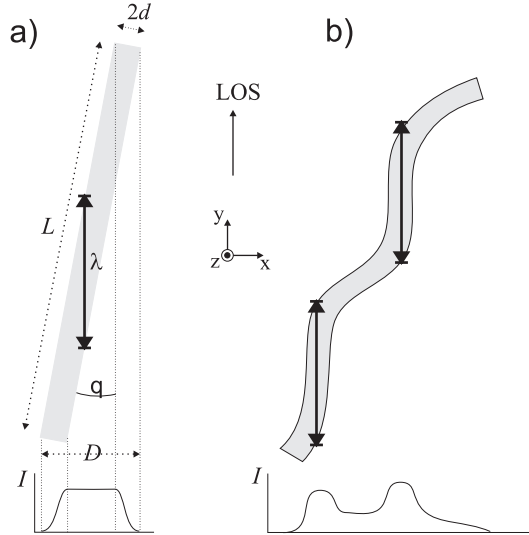


**Fig. 2.** Dependence of the width and morphology of the ray at a given height on the orientation/geometry of the current sheet: a) straight CS; b) wavy CS. The CS half-thickness is denoted by  $d$ , horizontal length (i.e., the length in  $xy$ -plane, see also Fig. 1) by  $L$ , the ray width by  $D$ , and the inclination to the line of sight (LoS) by  $\theta$ . The plasma-column length  $\lambda$  is drawn by thick double-arrow. At the bottom the intensity profile is sketched.

the characteristics of the reconnection jets depend also on the height. The main effect is transport of the dense plasma from lower heights upward, making the outflow jet much denser than the ambient corona (see Appendix). In this respect, the post-CME ray should be, to a certain degree, similar to coronal streamers.

Bearing in mind the geometry of the Petschek-type reconnection, the post-CME CS should show distinct morphological characteristics. It should be thinnest at the height of the diffusion region, getting wider with increasing height. In the homogeneous plasma the angle between the SMSs is determined by the inflow Mach number (Soward & Priest 1982; Vršnak & Skender 2005), the half-angle typically adding up to several degrees (Vršnak & Skender 2005). Thus, for the CS length of several solar radii, the Petschek-CS thickness (the distance between the SMSs) is on the order of 100 Mm. Note that in the case of the vertical CS in the solar corona, where the magnetic field diverges radially, the angle between SMSs should increase with the height even at uniform inflow Mach number (see Appendix), so the CS thickness should be somewhat larger than in the plane-symmetric case.

Further important characteristics of the post-CME CS that determine how it should look in coronagraphic images, are the horizontal length and the orientation with respect to the line of sight (Fig. 2). In this respect, it is important to note that the angle  $\theta$  between the plane of CS and the line of sight (LoS) has to be rather small, otherwise the CS would not appear as a distinct feature in coronagraphic images. This causes a “selection effect”, which can explain the fact that post-CME rays can be recognized only in a relatively small fraction of events (Webb et al. 2003).

In Fig. 2a we depict how the effective thickness  $D$  of the ray depends on the CS thickness  $2d$ , horizontal length  $L$ , and the angle  $\theta$ . On average, a ray should be thinner and brighter for smaller  $\theta$  (larger LoS column-length  $\lambda$ ). In Fig. 2b we illustrate how the variation of  $\theta$  along the LoS can lead to a complex appearance of the ray (see also Saez et al. 2007), i.e., a wavy CS would be seen by observer as a “multi-ray” structure. Note that the angle  $\theta$ , or its variation along the LoS, can vary in time and height, so the morphology of the structure can change in time and can be different at different heights.

### 3. Observations

#### 3.1. *SoHO/LASCO mass images*

For the analysis of the morphology and the column-density of post-CME rays we employ data provided by the Large Angle Spectroscopic Coronagraph (LASCO; Brueckner et al. 1995) on board SoHO. We focus on the LASCO-C2 images, covering the radial distance range from 2 to 6 solar radii ( $r_\odot$ ). In particular, we use the so-called mass images that are derived from LASCO base-difference images calibrated in units of solar brightness. These images show changes of the column-mass along the line of sight under the assumption that the structure lies in the plane of sky (for details we refer to Billings 1966; Poland et al. 1981; Vourlidas et al. 2000, 2002); bright pixels (positive values) represent areas where the column-mass is increased, whereas dark pixels (negative values) show depleted regions.

The initial sample of post-CME rays considered for the analysis consisted of eleven events. We emphasize that these rays were spotted while analyzing the associated CMEs for other purposes, i.e., the rays were chosen rather randomly. Thus, no attempt was made to analyze the occurrence rate of post-CME rays (for the criteria and statistical background we refer to Webb et al. 2003). Nevertheless, it should be noted that ray-like features in the

wake of CMEs are not uncommon, particularly bearing in mind specific circumstances under which a post-CME current sheet could be observed. That is, the level of post-CME activity should not be too high, current sheet has to be oriented at small angle with respect to the line of sight, it should be relatively stable, etc.

Inspecting the selected sample we noticed intermittent activity in most of the rays, manifested as changes of their shape, contrast, inclination, etc. These changes were either caused by coronal disturbances coming from remote eruptions, or were revealing internal activity, such as blob formation/ejection and/or outward propagating wave-like perturbations.

For a detailed analysis we chose three post-CME rays, observed on 8-9 January 2002, 18 November 2003, and 26 June 2005. The events of 18 November 2003 and 26 June 2005 were selected as examples of relatively stable rays. In both events we analyzed only one ray image (12:50 UT and 06:30 UT, respectively). On the other hand, the event of 8-9 January 2002 was showing a significant activity, similar to that in the remaining eight events. This event was selected to quantify the level of variability in post-CME rays, so we performed measurements at three different times (00:06, 06:06, and 12:06 UT). Note that rays in the selected exposures did not show significant blob-like features or similar inhomogeneities, although they might have been present in earlier and/or later times.

### 3.2. *The ray morphology*

In Fig. 3 we illustrate the variability of the ray morphology by showing two images of the ray that became recognizable a few hours after the east-limb CME eruption on 8 January 2002 (first appearance in LASCO-C2 at 17:54 UT). In Fig. 3a we first show a simple ray pattern that was recorded half a day after the eruption. Four hours earlier, the ray had a complex form consisting of three radial substructures (Fig. 3b); this “multi-ray” pattern could be a result of a wavy current sheet, as illustrated in Fig. 2b. Morphological changes of this kind, developing on the time scale of hours are a common characteristic of post-CME rays, since they were present in nine out of eleven events from our initial sample.

The estimates of the ray width and the column-mass excess are based on the LASCO-C2 mass-images (Fig. 3 left), which provide for each pixel the difference  $\Delta m$  between the column-mass in the actual image and the reference image. In the right-hand panels of Fig. 3 we show two mass-difference profiles  $\Delta m(y)$ , where  $\Delta m$  is expressed in g/pixel, while the abscissa, corresponding to the  $y$  coordinate of LASCO images, is represented in pixels. The profiles shown were measured in the LASCO-C2 difference-images along the bin marked by white lines in the left panel of Fig. 3, i.e., roughly perpendicular to the ray direction. The bin is 10 pixels wide, and the profile shows  $\Delta m$  averaged over the bin width. Pixels with  $\Delta m = 0$  represent areas where the column-mass remained the same as in the reference image. Note that the mass astride the rays is depleted ( $\Delta m < 0$ ), probably due to the CME-associated coronal expansion, usually seen as coronal dimming when the eruption is launched from regions on the solar disc. The depletion might be partly caused also by the presumed inflow into the current sheet.

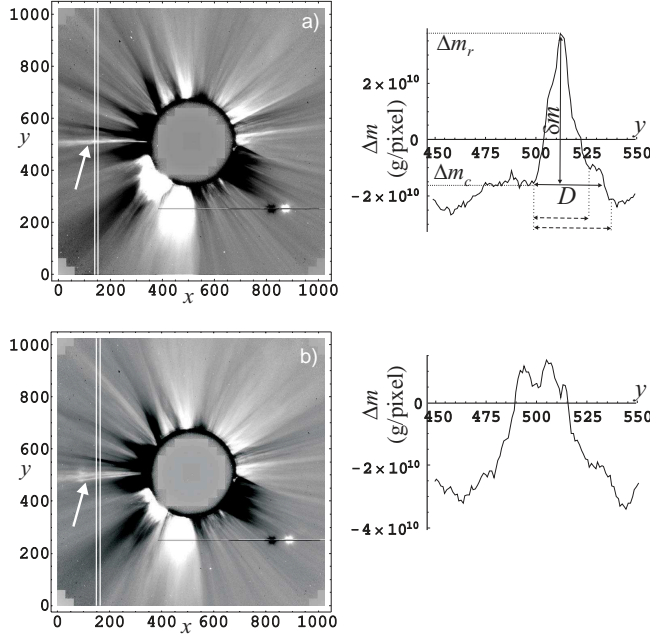


**Fig. 3.** a) Simple post-CME ray (9 January 2002 at 06:06 UT); b) Complex ray consisting of three radial substructures (9 January 2002 at 02:30 UT). The ray is marked by white arrow. The scale of the LASCO-C2 images is given in pixels (1 pixel corresponds to 11.9 arcsec). The column-mass profiles measured along the bin marked by white lines are shown in the right-hand panels (abscissa scale in pixels). Estimates of the ray width,  $D$ , and column-mass excess,  $\delta m$ , are indicated in a). Dashed arrows indicate the lower and upper limit of  $D$ .

Given the working hypothesis, where the ray is considered to be the reconnection outflow jet of a large-scale Petschek-like bifurcated current sheet, we are interested in the column-mass excess of the ray,  $\delta m$ , defined as the difference between the peak in the ray column-mass  $\Delta m_r$  and the column-mass in the adjacent corona  $\Delta m_c$ . In other words,  $\delta m$  determines the difference of column-mass associated with the current sheet and the inflow region ( $\delta m = \Delta m_r - \Delta m_c$ ; see the right-hand panel of Fig. 3a). The ray width  $D$  is measured as the full width of the ray structure in the mass-difference profile (Fig. 3a right). The main source of error in estimating  $\delta m$  and  $D$  is in determining the value  $\Delta m_c$ , since this value is frequently different on opposite sides of the ray (Fig. 3a right). Thus, we estimated the upper and lower limit (dashed arrows in Fig. 3a right), and these measurements gave us the error bars plotted in Fig. 4.

The measurements illustrated in Fig. 3 were performed in five images of post-CME rays over the LASCO-C2 range of heights to estimate radial dependence of relevant ray parameters. The measured rays are marked in the mass-images shown in the left column of Fig. 4 (hereinafter denoted as rays a–e). In the second column of Fig. 4 the ray widths, expressed in units of the solar radius  $r_\odot$ , are presented as a function of the radial distance,  $D(R)$ , where  $R = r/r_\odot$ . The ray in Fig. 4a is characterized by “multi-ray” structure, so we measured only the central feature, which was the most prominent element of the structure.

Inspecting the graphs one finds that in the distance range  $R = 2–2.5$  the widths span between 0.1 and 0.4  $r_\odot$  (mean 0.26). In the range  $R = 5–6$  the widths increase to 0.4–



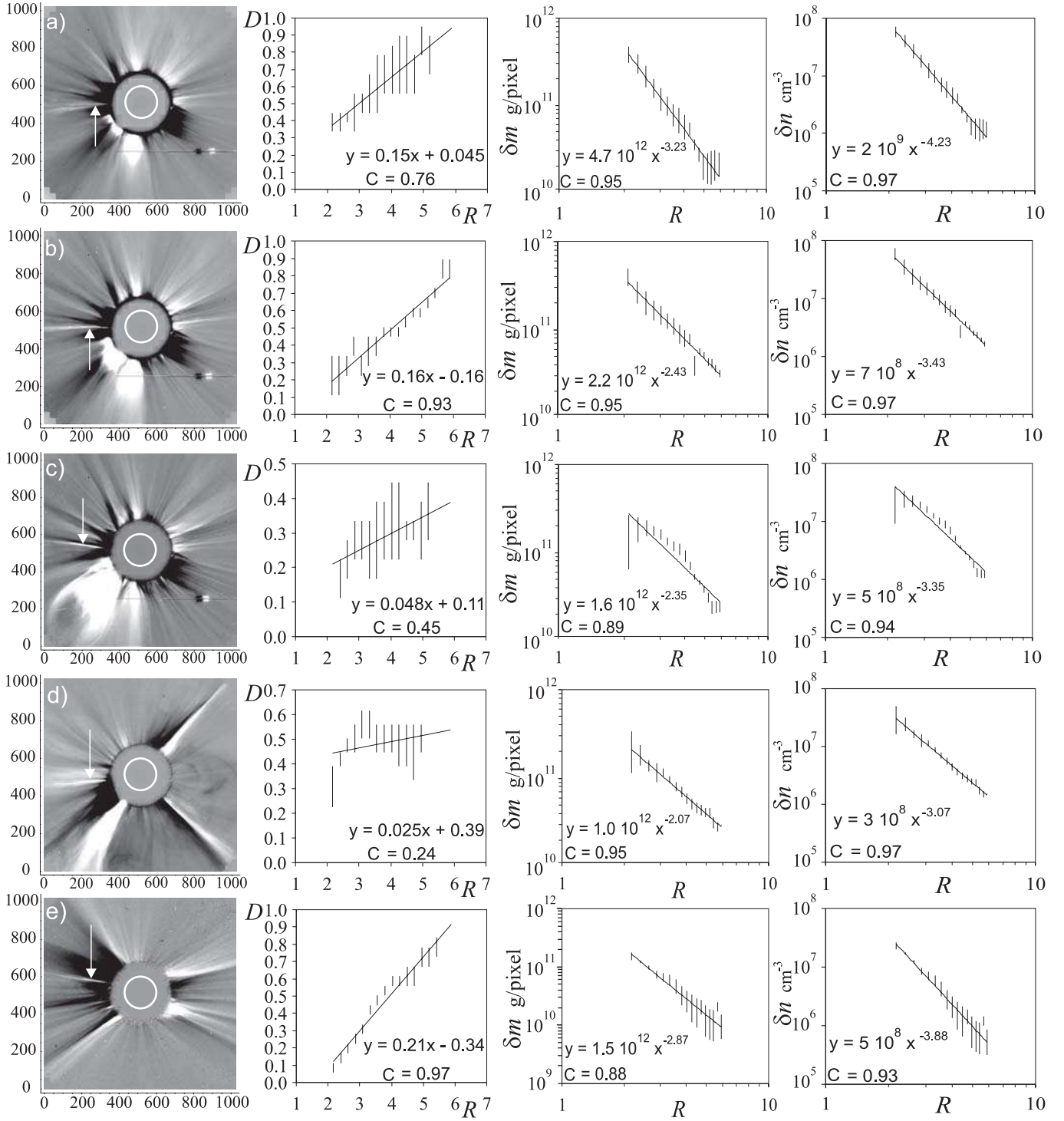


**Fig. 4.** The five measured post-CME rays (indicated by arrows in the full-resolution LASCO-C2 images shown in the first column): a)–c) 9 January 2002 at 00:06, 06:06, and 12:06 UT, respectively; d) 18 November 2003 at 12:50 UT; e) 26 June 2005 at 06:30 UT. In the second, third, and fourth column we show the ray width, column-mass excess, and the density excess, as a function of the radial distance. The widths and radial distances are expressed in units of the solar radius. The least-square fits are shown in the insets, together with the correlation coefficient  $C$ .

$0.9 r_{\odot}$  (mean 0.7). The widths we found at  $R \sim 2$  are more than twice larger than found by Webb et al. (2003) who analyzed the coronagraph data on board the Solar Maximum Mission (SMM): converting their values of the width expressed in degrees, into units of the solar radius at the corresponding heights, we find that the mean width reported by Webb et al. (2003, see Tabs. 2 and 3 therein) is  $0.09 r_{\odot}$  in this height range. The difference may be related to the lower sensitivity of SMM.

### 3.3. The ray density

In the third column of Fig. 4 we show the radial dependencies of column-mass excesses  $\delta m(R)$ , expressed in g/pixel. Inspecting the graphs  $\delta m(R)$  we find that the slopes of the fitted power-law functions range from  $-2.1$  to  $-3.2$ . The average value adds up to  $-2.6 \pm 0.5$ .

The column-mass excess  $\delta m$  was converted to the number-density excess  $\delta n$  by assuming that, due to the spherical geometry, the column length increases proportionally with the radial distance,  $\lambda \propto R$ . In particular, we used  $\lambda_0 = 100$  Mm at  $R = R_0 = 2.16$  (the lowest height of measurements). The outcome is presented in log-log graphs in the fourth column of Fig. 4, together with the power law fits. Note that some other choice of  $\lambda_0$  would shift vertically the  $\delta n(R)$  dependence, without changing the slope in log-log graph. The slope would change only if some other radial dependence  $\lambda(R)$  would be applied, e.g., the angle  $\theta$  might be height-dependent.

Inspecting the graphs  $\delta n(R)$  in Fig. 4 we find that the slopes of the fitted power-law functions range from  $-3.1$  to  $-4.2$ , the average value adding up  $-3.6 \pm 0.5$ . [We pay special attention to the slope of the fit, since it does not depend on the presumed value of  $\lambda_0$ , so it can be directly compared with the model results (Sect. 4.1).] In this respect it is important to note that in the case of the smallest slope in the sample, the ray width becomes approximately constant beyond  $R \approx 3$ , indicating a possible decrease of  $\theta$  with the height, i.e., the increase of  $\lambda$ . This would imply that in this case the densities are overestimated at larger heights, since  $\delta n \propto \delta m/\lambda$ , i.e., the true slope of  $\delta n(R)$  is probably somewhat steeper.

Since the evaluation of the density excess depends on the choice of the column length  $\lambda$ , in Fig. 5 we present an estimate of the number of electrons per unit length of the ray, which is a parameter independent of  $\lambda$ . If we approximate the mass-difference profiles across the ray by triangular profiles, the mass-excess per unit length of the profile amounts to  $M = D\delta m/2$ , from which we evaluate the electron-number excess per unit length of the ray,  $N_e$ .

Inspecting Fig. 5a, where  $N_e(R)$  is presented separately for all five rays from Fig. 4, we find that  $N_e(R)$  either decreases (rays [a], [b], and [d]) or stays roughly constant (rays [c] and [e]). When averaged, the data from Fig. 5b show a dependence similar to that obtained by Ciaravella & Raymond (2008), who found that after a decrease at low heights, the value of  $N_e$  becomes approximately constant. Comparing their Fig. 8 with our Fig. 5b we find that the numbers and the trends are similar. However, the difference is the radial distance at which  $N_e(R)$  becomes constant: according to results by Ciaravella & Raymond (2008) this happens at  $R \approx 2$ , whereas in our case the transition occurs at  $R \approx 4$ . In Fig. 5b we

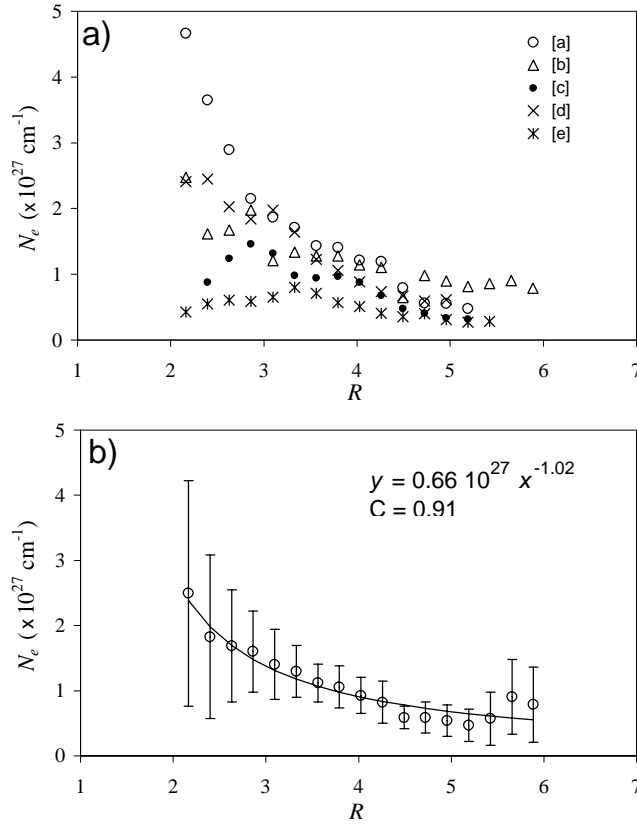


**Fig. 5.** Number of electrons per unit length of the ray,  $N_e(R)$ : a) presented separately for the five rays shown in Fig. 4 (measurements are labeled in the legend, following the sequence in Fig. 4); b) averaged over the five rays (error bars represent standard deviations), shown together with the power-law fit.

present also the power-law fit, showing that the overall trend could be described as well by  $N_e \propto R^{-1}$ .

### 3.4. Coronal flows

Coronal regions beneath CMEs are generally characterized by highly dynamical intricate structures, revealing complex magnetoplasma flows and waves. Consequently, it is difficult to find persistent systematic flow patterns, especially in periods of increased solar activity, when disturbances from other CMEs affect the coronal region of interest. This also holds for flow patterns associated with post-CME rays, which show permanent morphological changes and are strongly affected by disturbances from distant CMEs.

Yet, in certain situations some characteristic flows could be identified. Most frequently, outward-moving inhomogeneities along the ray are observed, usually having velocities of several hundred  $\text{km s}^{-1}$  (e.g., Ko et al. 2003; Lin et al. 2005). Such motions are often interpreted in terms of the reconnection outflow, which may or may not be characterized by the Alfvénic speed (for a discussion we refer to Bárta et al. 2008, and references therein). In this respect we note that sometimes signatures of shrinking loops are also observed in the wake of CMEs (e.g., Sheeley & Wang 2002; Sheeley et al. 2004; Sheeley & Wang 2007, and references therein), consistent with decelerated reconnection downflows.

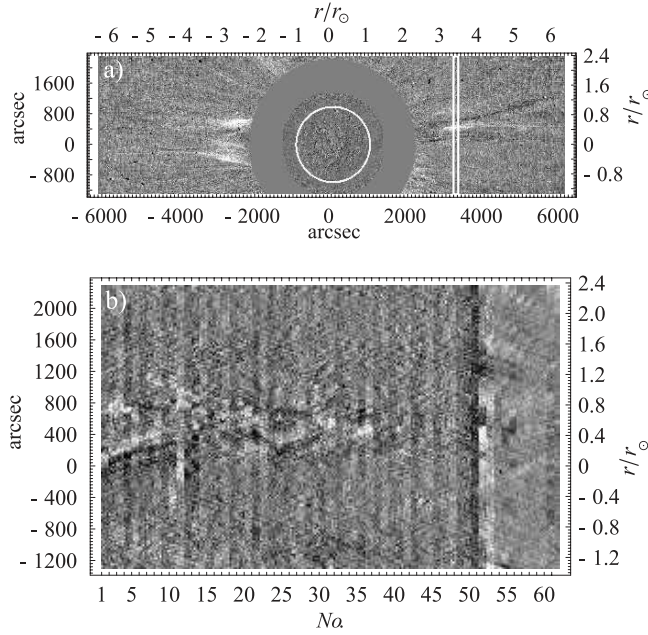


**Fig. 6.** a) LASCO-C2 running-difference images of the west-limb ray of 8 January 2002 (13:54 UT), revealing the inflow into the ray. The slice used in the stack-plot shown in b) is outlined by white rectangle centered at  $x = +3.34 r_{\odot}$ . b) Stack-plot composed of slices taken from successive running-difference images;  $x$ -axis represents the ordinal number of the LASCO image for 8 January 2002.

Compared to reconnection outflows, detecting signatures of reconnection inflows is much more difficult. A possible example was reported by Yokoyama et al. (2001), based on the observations by the EIT/SoHO. Another example was presented by Lin et al. (2005), who employed data from EIT and UltraViolet Coronagraph Spectrometer (UVCS) on board SoHO. Recently, Bemporad et al. (2008) reported a “side-reconnection” in the aftermath of a CME, induced by the CME expansion: from the detection of two converging reconnecting features at  $1.7 r_{\odot}$  (probably the CME flank and the streamer boundary) the authors inferred an inflow speed of 3–4 km/s, close to the 5 km/s derived by Yokoyama et al. (2001).

In Fig. 6 we present a stack-plot showing an example of the reconnection-inflow pattern observed above the west limb on 8 January 2002 in the LASCO-C2 field-of-view. Note that this post-CME feature is not the ray of 8-9 January 2002 presented in Figs. 3 and 4, which was on the opposite side of the solar disc. This west-limb event was not observed by UVCS, i.e., we do not know if it was characterized by the Fe XVIII emission, which is one of criteria for identifying post-CME current sheets. It should be stressed that we could not find a clear/measurable signature of reconnection inflow in the three post-CME rays analyzed in Sects. 3.2. and 3.3. In these events no suitable inhomogeneities could be identified to provide tracing of plasma motion in the inflow region (to be discussed in Sect. 5).

The west-limb ray presented in Fig. 6, formed after a faint ejection first observed in LASCO-C2 at 02:54 UT on 8 January 2002 (not listed in the LASCO CME catalog). Each stack represents the cut along a line parallel to the  $y$ -axis of a given LASCO-C2  $512 \times 512$ -pixel running-difference image, showing the pixel-intensities in the range  $x = 3.30 - 3.38 r_{\odot}$ .

Note that the ray was oriented very close to the  $x$ -axis of LASCO images, i.e., the stacks are roughly perpendicular to the ray direction. The stack-plot contains all images recorded on 8 January 2002 (denoted by ordinal number at the  $x$ -axis of the stack-plot; the time cadence is on average 24 min).

The black/white stripes converging towards the ray location, located at  $y \sim 400'' \sim 0.41r_{\odot}$ , clearly show inflows into the ray. The corresponding velocities in the left part of the stack-plot are found in the range  $15\text{--}25\text{ km s}^{-1}$  (mean  $19 \pm 4\text{ km s}^{-1}$ ). Such velocities are several times higher than  $5\text{ km s}^{-1}$  reported by Yokoyama et al. (2001). After the slice No. 50 (18:54 UT), the stack-plot reveals effects of a large-scale perturbation from another CME, which occurred above the E-limb. Note that the “push” caused by the perturbation increased the inflow speed, now ranging from 25 to  $30\text{ km s}^{-1}$  (mean  $27 \pm 5\text{ km s}^{-1}$ ).

Finally, it should be noted that we also observed intermittent downflows in the form of shrinking loops (similar to that reported by Sheeley et al. 2004), starting from  $R \sim 3$ . At larger heights, outflows could be recognized, sometimes showing a pattern like in disconnection events (e.g., Webb & Cliver 1995; Simnett et al. 1997; Wang et al. 1999). This implies that the diffusion region in this event was located around  $R \sim 3$ , i.e., much higher than in the events shown in Fig. 4.

## 4. Comparison with the model and previous studies

### 4.1. Comparison with the model results

In Fig. 7a we present a comparison of measurements presented in 4th column of Fig. 4 with the model-dependencies  $\delta n(R)$  derived in the Appendix. In particular, we present the model results based on the isothermal ( $T = 10^6\text{ K}$ ) Parker (1958) solar wind model (see also Mann et al. 1999a). For the magnetic field  $B(R)$  we take the empirical coronal magnetic field scaling established by Dulk & McLean (1978). Note that data [a], [b], [d], and [e] are slightly shifted in  $R$ -coordinate (symmetrically with respect to [c]) to avoid overlapping. Figure 7a clearly shows that the observations fit well to the model curves (as stated in Sect. 3.3 the choice of the column length  $\lambda_0$  only shifts the values up or down, but does not change the slope). Comparing the trend of the data we see that the slope corresponds much better to the model slopes for the CSs than for the ambient corona. Furthermore one finds that the CS densities are more than one order of magnitude larger than that in the ambient corona.

In Fig. 7b we present the measured average density excess  $\overline{\delta n}(R)$  (circles with error bars represent the mean values from Fig. 7a with the associated standard deviations) and the corresponding power-law fit, compared with the CS model dependencies. The observational data show the dependence  $R^{-3.6}$ , whereas in the same height range the CS model data show  $\sim R^{-3.0} - R^{-3.2}$  and the quiet-corona model behaves as  $R^{-4.3}$  (see Appendix).

### 4.2. Ray densities from previous studies

Post-CME rays were studied in a number of papers, employing various techniques to estimate their density. In Table 1 we present an overview of the spectrographic results obtained

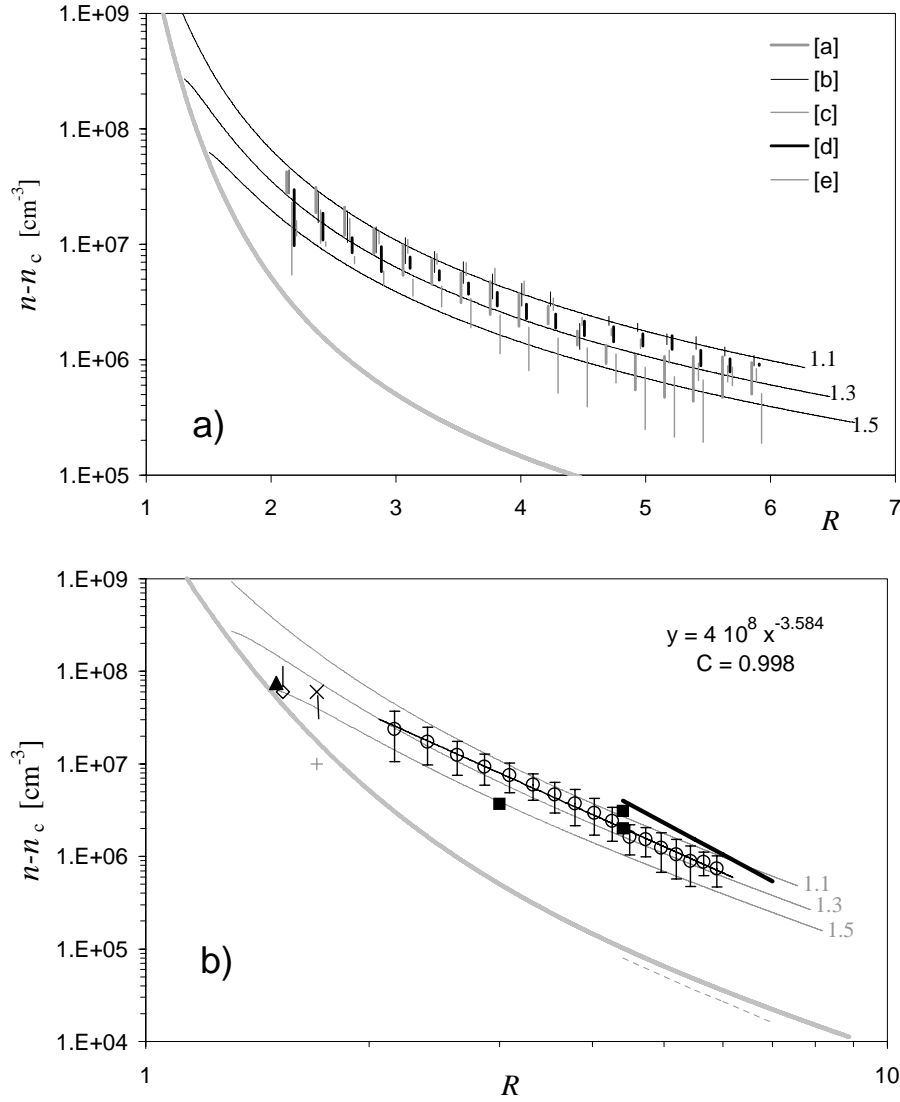


**Fig. 7.** a) Comparison of the density-excess measurements presented in the right hand column of Fig. 4 with the model results (thin black lines labeled by the heliocentric distance of the diffusion region,  $R_x$ ). Measurements are labeled in the legend, following the sequence in Fig. 4. The thick-gray line shows the density model of a quiet  $10^6$  K corona (Mann et al. 1999a). b) The mean values of the data presented in (a), shown by circles with error bars and the corresponding power-law fit (written in the inset), compared with the model results and the values from previous studies reviewed in Sect. 4.2 (diamond – Ko et al. (2003); triangle – Ciaravella et al. (2002); squares – Ko et al. (2003); cross – Bemporad et al. (2006)).

from UltraViolet (UV) spectra of five post-CME rays (dates are given in the header row) reported by Ciaravella et al. (2002), Ko et al. (2003), Raymond et al. (2003), Lee et al. (2006), Bemporad et al. (2006), and Ciaravella & Raymond (2008). In the last column we also present the unpublished results by Schettino et al. (2008, to be submitted).

All rays listed in Table 1 were characterized by the presence of the narrow Fe XVIII emission. UV spectra of rays have been obtained with the UltraViolet Coronagraph Spectrometer (UVCS; Kohl et al. 1995) on board SoHO. The spectrometer observes through a narrow entrance slit  $42'$  long and up to  $84''$  wide. The slit can be located at

**Table 1.** Spectrographic results on the UV current sheets.

	1998 Mar 23 <sup>1</sup>	2002 Jan 8 <sup>2</sup>	2002 Apr 21 <sup>3</sup>	2002 Nov 26 <sup>4</sup>	2003 Nov 4 <sup>5</sup>	2003 June 2 <sup>6</sup>
CME 1st-LASCO	09:33:36	17:54:05	01:27:20	17:06:21	19:54:05	08:54:05
CME speed (km s <sup>-1</sup> )	403	1794	2393	479	2657	980
Flare	N	Ybl*	X 1.5	N	X 30.8	M 3.9
AR No.	—	9782/85	9906	—	10486	10365
LASCO CS	N	2 days	N	N	~ 20 h	6.5 h
CS obs. start	16:00:30	17:48/Jan 10	00:45:34	18:39:15	20:03:50	09:40:44
CS obs. height	1.51 (–1.38)	1.53	1.62	1.61	1.69	1.68
CS FWHM width ( $r_{\odot}$ )	0.1	0.2	0.3	0.4	0.2–0.1	0.3
CS full width ( $r_{\odot}$ )	0.4	0.4	0.6	0.8	0.5–0.2	0.35
CS LoS depth ( $r_{\odot}$ )	0.06	0.2	—	0.5	0.1	0.1
CS obs. duration	20 h	10 h	14 min	2.3 days	~ 17 h	6.3 h
CS temp. (10 <sup>6</sup> K)	5	3–4	5	8–3	8–4	7
CS density (10 <sup>7</sup> cm <sup>-3</sup> )	5–10	≤ 4	—	6.5–7.5	7–10	1

1 - Ciaravella et al. (2002);

2 - Ko et al. (2003);

3 - Raymond et al. (2003); Lee et al. (2006);

4 - Bemporad et al. (2006);

5 - Ciaravella &amp; Raymond (2008)

6 - Schettino et al. (2008, to be submitted)

\* Ybl = Yes (behind the limb)

any polar angle and at heliocentric distances from 1.5 up to  $10 r_{\odot}$ . UVCS can image spectra of the solar corona in the range 945–1270 Å (473–635 Å in the second order).

The first five rows of Table 1 specify the associated CME/flare events: the first appearance of the CME in the LASCO-C2, the CME mean speed, the soft X-ray importance of the flare if observed, the active region label, and duration of the LASCO-ray if observed, respectively.

The next eight rows concern the ray characteristics as detected in the UV spectra: the time of the first detection of the ray by UVCS, the height at which the spectrograph slit intersects the ray, the ray width along the UVCS slit expressed in units of  $r_{\odot}$  (both the full-width at half-maximum and the full width are presented), the estimate of the LoS depth, duration of the ray UVCS observations, and finally, in last two rows we present the ray temperature and density.

The ray UVCS densities are presented in Fig. 7b, together with the density-excess measurements presented in Sects. 3.3 and 4.1. The estimate based on the UVCS spectra reported by Ko et al. (2003) is indicated by the diamond symbol. The column-length was assumed therein to be 140 Mm which was taken to be the same as the FWHM of the spatial profile of the FeXVIII  $\lambda 974$  emission across the post-CME rays. Such a column-length is

about 2 times larger than the value we would get for this height by the scaling that was applied in Sect. 3. Thus, to adjust the values to our  $\lambda_0$  the density has to be multiplied by a factor of 2 (indicated by vertical bar attached to the diamond symbol in Fig. 7b).

The density reported by Ciaravella et al. (2002), also estimated from the UVCS data, is shown by the black triangle. Ciaravella et al. (2002) estimated the CS density at  $R = 1.5$  to  $5 - 10 \times 10^7 \text{ cm}^{-3}$  assuming the column length of 40 Mm. After adjusting to the column-length equivalent to that we used in Sect. 3 (required increase is around 20%), we find the equivalent density around  $6 \times 10^7 \text{ cm}^{-3}$ .

The density inferred by Bemporad et al. (2006) from the spectral observations of the face-on current sheet of 26 November 2002 is shown by the black cross. The attached vertical bar indicates that the density could be lower if a larger current sheet thickness would be assumed. The gray plus symbol represents the estimated density of the ambient coronal plasma.

In Fig. 7b we also show (black squares) the density excess data based on the ray and coronal densities estimated by Ko et al. (2003) employing the LASCO-C2 observations and using the Thompson scattering function (Billings 1966). In estimating the ray density at  $R = 4.4$  Ko et al. (2003) assumed the column-length of  $\sim 250$  Mm, which is about 1.2 times larger value than we used at the same height. Thus, adjusting their results to our column-length would result in 1.2 times lower density.

Finally, in Fig. 7b the results based on the polarization-brightness measurements performed by Poletto et al. (2008) are presented. The thick black line represents the density excess  $\delta n$  re-evaluated from Fig. 9 of Poletto et al. (2008) by applying column-lengths consistent with those applied in Sect. 3. The ray data drawn by the thick line fit very closely to our measurements, whereas the “quiet corona” data (thin gray dashed line) are very close to the model densities.

The power-law fit to all data (adjusted to the same  $\lambda_0$ ) shown in Fig. 7b has the slope  $R^{-3.3}$  (without the  $\lambda_0$  adjustment would add up to  $R^{-3.0}$ ). This is quite close to the model slopes found in the radial distance range  $1.5 - 7 r_\odot$ , characterized by the power-law exponents  $3.0 - 3.2$  for  $R_x = 1.1 - 1.5$  and the Dulk & McLean (1978) magnetic field.

## 5. Discussion and conclusion

The empirical characteristics of post-CME rays we summarize as follows:

1. rays often show activity in the form of outflowing features, morphological changes, and changes of the inclination; sometimes reconnection inflows are observed;
2. the width of rays increases with height, from  $\sim 0.1 - 0.3 r_\odot$  at  $R \sim 2$  to  $\sim 0.4 - 0.8 r_\odot$  at  $R \sim 6$ .
3. densities found in rays are at least several times (up to more than one order of magnitude) larger than in the ambient corona in the considered height range;
4. coronal regions surrounding rays are depleted;
5. on average, the number of electrons per unit length of the ray,  $N_e$ , first decreases with the height, and then, at larger heights becomes approximately constant;



6. temperature of rays in the range  $R \sim 1.5 - 1.7$  spans from 3 to 8 MK, i.e., it is several times larger than in the “normal” corona, with a tendency to decrease in time.

The nature of the coronagraphic white-light ray activity is twofold. The formation of fine structure elements, mostly blob-like features, and their outward motion at speeds in the range  $100 - 1000 \text{ km s}^{-1}$ , seems to be the most common internal activity. It could be interpreted in terms of the current sheet tearing, resulting in the formation and outward ejection of plasmoids (e.g., Bárta et al. 2008; Riley et al. 2007, and references therein). On the other hand, changes of the ray inclination, as well as morphological changes that could be attributed to changes of the ray geometry, seem to be caused by the large-scale magnetic field evolution in the wake of the CME. In some cases this type of activity is caused by perturbations coming from distant eruptions, most likely the large-amplitude waves or shocks.

As stated in item 2, the width increases on average by about  $0.4 r_{\odot}$  over the distance of  $4 r_{\odot}$ , i.e., the width is roughly proportional to the radial distance. Following our interpretation of rays in terms of the reconnecting current sheet, the ray boundaries should outline the slow mode shocks. Given the model presented in the Appendix, in particular Fig. 8, it can be concluded that the slow mode shocks are oriented very close to the radial direction, i.e., that the angle denoted in Fig. 8 as  $\phi$ , is very small. Since the angle  $\phi$  (expressed in radians) equals to the inflow Alfvén Mach number reduced by the factor  $n_2/n_1$  that represents the density jump at the slow mode shock (the value of  $n_2/n_1$  depends on  $\beta$ , and should be around 2; see Vršnak & Skender 2005), one finds that the inflow Mach number is low, most likely in the order of 0.01 or less. [For larger values,  $\phi$  would be large enough to make the “super-radial” widening of the ray measurable.] This may be the reason why inflows like those shown in Fig. 6 are rarely observed.

Note that the situation shown in Fig. 6 is different from the previously described “stationary” pattern. In this case we see distinct elongated features inflowing from both sides towards the ray axis of symmetry. Thus, these features cannot be interpreted as CS boundaries, i.e., signatures of the slow mode shocks, but rather they represent coronal density inhomogeneities aligned with the magnetic fieldlines. These features are inclined from the radial direction, i.e., show the “super-radial” orientation. When observed in pairs, they form a V-pattern roughly symmetric with respect to the ray axis. Thus, these substructures most likely outline the magnetic field inflowing into the current sheet. In such a situation the angle (expressed in radians) between the fieldline and the axis of symmetry is equal to the inflow Alfvén Mach number  $M_A$  (e.g., Vršnak & Skender 2005). In the event shown in Fig. 6, we estimate this angle to a few degrees, so we can take  $M_A \sim 0.02 - 0.05$ . Bearing in mind that the inflow speed was estimated to  $\sim 20 \text{ km s}^{-1}$ , this would correspond to the Alfvén speed of  $400 - 1000 \text{ km s}^{-1}$ , which seems reasonable for this height range (see, e.g., Vršnak et al. 2004).

The main physical characteristics of post-CME rays are their mass/density excess and increased temperature (Table I). This, as well as the morphology and flows, can be explained in terms of the reconnection outflow-jet, being the structural element of the vertical current sheet that forms in the wake of a CME. The measured values of the CS density and the

temperature provide also an estimate of the ambient coronal magnetic field, since the external magnetic pressure is roughly equal to the gas pressure in the outflow region (see, e.g., Appendix in Aurass et al. 2002). Using the values  $n_{CS} = 5 - 10 \times 10^7 \text{ cm}^{-3}$  and  $T_{CS} = 5 - 8 \text{ MK}$ , we find for the ambient magnetic field  $B_c \sim 0.9 - 1.7 \text{ gauss}$ . Such a magnetic field is consistent with the empirical scaling  $B = 0.5(R - 1)^{-1.5}$  established by Dulk & McLean (1978), which gives  $B \sim 0.85 - 1.41 \text{ gauss}$  for the radial distance range  $R = 1.5 - 1.7$ . Similarly, using the relationship between the temperature jump at SMSs and the external plasma-to-magnetic pressure ratio,  $T_2/T_1 = 1 + 0.4/\beta$  (see Eq. 12 in Aurass et al. 2002), one can estimate the value of  $\beta$  in the inflow region. Applying  $T_2/T_1 \lesssim T_{CS}/T_c = 2 - 8$ , we find  $\beta \gtrsim 0.4 - 0.06$ . Such values are roughly consistent with those expected for the active region corona in this height range (Gary 2001).

The results of the model, based on the quasi-stationary Petschek (1964) reconnection regime, are consistent with the observed density excesses. At the standing slow mode shocks, formed by the CS inflow, the plasma is heated, compressed, and accelerated/deflected to form the upward directed reconnection jet. In this way the dense plasma from low corona is transported to larger heights, causing the observed density excess. Model results show that the density can be increased by more than one order of magnitude, which is consistent with observations. However, it should be noted that the observed values depend on the assumed value of the LoS CS-depth  $\lambda_0$ . Our results indicate that  $\lambda_0$  is in the order of 100 Mm, and that the plane of the observed rays is inclined at small angle with respect to the LoS.

The parameter that does not depend on the LoS CS-depth, or the CS orientation, is the number of electrons per unit length of the CS, which we denoted in Sect. 3.3 as  $N_e$ . The measurements show that  $N_e(R)$  either decreases, or is approximately constant. On average,  $N_e(R)$  first decreases, to become approximately constant at  $R_c \sim 4$ . Given our observations, as well as the observations by Ciaravella & Raymond (2008), it seems that  $R_c$  is different in different events.

Bearing in mind the equation of continuity, there are two effects that determine the radial dependence of  $N_e$ . One is the radial dependence of the reconnection-outflow velocity, and another one is the contribution of the inflowing plasma. For example, if the outflow speed would be constant, the value of  $N_e$  would be increasing monotonously with the height due to the cumulative supply of the plasma through the SMSs (more and more inflowing plasma joining to the outflow). On the other hand, if the inflow contribution is negligible (as it is at large heights), then a decelerated outflow would be associated with increasing  $N_e(R)$ , whereas the accelerated outflow would lead to a decreasing  $N_e(R)$ .

Inspecting outcomes for various model inputs, we found that regardless on the model details, in the vicinity of the diffusion region  $N_e(R)$  increases steeply due to a strong effect of the plasma inflow. At larger heights, beyond  $\sim 0.5 r_\odot$  above the diffusion region, the behavior of  $N_e(R)$  becomes dependent on the model input. A match with the observations (decreasing  $N_e(R)$  followed by  $N_e \sim \text{const.}$ ) is found only for cases where the Alfvén velocity and the solar wind speed increase in the given height range, and only if the diffusion region is below  $R \sim 1.4$ . Given that the power-law fit presented in Fig. 5b quite well describes the  $N_e(R)$  dependence as  $N_e \propto R^{-1}$ , would imply that the outflow velocity

increases approximately as  $v_{out} \propto R$ . However, note that the last three data-points in Fig. 5b might indicate that  $N_e$  starts to increase gradually beyond  $R \sim 5$ . Such a behavior is found in all of the considered model options, i.e., after the solar wind speed becomes approximately constant and the Alfvén velocity starts decreasing, the value of  $N_e$  gradually increases with the radial distance.

In this respect, it should be stressed that the model results generally depend on the applied coronal density and magnetic field model. On the other hand, the  $N_e(R)$  measurements are burdened by large errors in estimating the ray width  $D$ . So, since the comparison of the observed and the calculated  $N_e(R)$  might lead to ambiguous conclusions, it turns out that the most reliable model-parameter to be compared with observations is the slope of the  $n_{CS}(R)$  dependence, which should be less steep than the slope of the ambient  $n_c(R)$ , regardless on the model details. Comparing the calculated and observed slopes we find a very good correspondence.

Finally, the model predicts a decrease of the density excess in time, due to the rise of the diffusion region height. Bearing in mind that this rise is slow, it is to be expected that the decrease of the density excess should be slow too. Indeed, we did not detect a decrease of the ray density in 12 hour interval analyzed in the ray of 9 January 2002. However, note that a decrease of the density was reported by Ciaravella & Raymond (2008) in the event of 4 November 2003. From their Table 1 we find that the density decreased by  $\sim 40-50\%$  in about 2 hours. According to our model, such a decrease would correspond to an increase of the diffusion region height for  $\Delta R \sim 0.1$ , which would correspond to the rise speed in the order of  $10 \text{ km s}^{-1}$ . On the other hand, given the accuracy of our density estimates ( $\sim 50\%$ ), we infer that in the event of 9 January 2002 the rise speed of the diffusion region was less than  $2 \text{ km s}^{-1}$ .

## Appendix

The overall geometry of the post-CME ray, assumed to be a signature of the bifurcated reconnecting current sheet, is shown in Fig. 1. The diffusion region, where the magnetic field lines reconnect, is located at the radial distance  $R_x$ . The oppositely directed field lines merge at the velocity  $v_{in}(R)$ , bringing into the reconnection outflow jet (the ray) the coronal plasma of the density  $n_c(R)$ . We assume that the merging velocity is faster than the local slow-mode speed, so the slow mode shocks (SMSs) form in between the two inflows, bounding the reconnection outflow like in the Petschek (1964) reconnection model.

Given the spherical geometry of the corona, the flow velocity vector in the inflow region can be represented as a superposition of the radial component (corresponding to the solar wind speed  $v_{sw}$ ) and the “horizontal” component  $v_{in}$  (direction of the unit vector  $\hat{\vartheta}$  shown in the lower-right corner of Fig. 8), as depicted in Fig. 1b.

In the stationary state the relation  $\nabla \times \mathbf{E} = 0$  must be satisfied, to provide  $\partial \mathbf{B} / \partial t = 0$ . In a spherical coordinate system (see the lower-right corner of Fig. 8) this implies  $\partial(rE_{\hat{\varphi}}) / \partial r = 0$ , i.e.,  $Rv_{in}B = \text{const.}$  For the ambient coronal magnetic field  $B(R)$  we take the empirical model by Dulk & McLean (1978) and the simple analytical model by Mann et al. (1999b) [see also Vršnak et al. (2002)], which then defines  $v_{in}(R)$ .

We denote the angle between the radial direction and the slow mode shock (Fig. 8) as  $\phi(R)$ . Taking into account the continuity equation across the SMS

$$v_{\text{in}}\rho_c\Delta R = v_{\text{out}}\rho_{\text{SMS}}\Delta R\phi, \quad (1)$$

where  $v_{\text{out}} \sim v_A + v_{\text{sw}}$  (Skender et al. 2003; Vršnak & Skender 2005), we find

$$\phi = \frac{\rho_c}{\rho_{\text{SMS}}} \frac{v_{\text{in}}}{v_A + v_{\text{sw}}}, \quad (2)$$

which defines the geometry of the SMSs.

For the coronal density  $\rho_c(R)$  we use the isothermal solar wind model by Parker (see Mann et al. 1999a) using for the temperature  $T_c = 1, 1.5$ , and 2 MK, which provides also the corresponding solar wind speed  $v_{\text{sw}}(R)$ . This, together with the previously defined  $B(R)$ , also defines the ambient coronal Alfvén velocity  $v_A(R)$  and plasma-to-magnetic pressure ratio  $\beta(R)$ , both governing the jump relations at the SMS. Assuming that the guiding field is negligible, the density and temperature jump at SMS can be expressed as:

$$\frac{\rho_{\text{SMS}}}{\rho_c} = \frac{5(1+\beta)}{2+5\beta}, \quad (3)$$

$$\frac{T_{\text{SMS}}}{T_c} = 1 + \frac{2}{5\beta}, \quad (4)$$

(Aurass et al. 2002; Skender et al. 2003; Vršnak & Skender 2005), which determines the density and the temperature of the plasma inflowing into the reconnection outflow jet at a given  $R$ .

At a given radial distance  $R$  the density of the reconnection outflow is determined by the flow carried from lower heights and by the flow carried across the SMS. Bearing in mind the geometry depicted in Fig. 8, the continuity equation (mass conservation) can be written in the form:

$$\rho_{i+1}^{\text{out}} v_{i+1}^{\text{out}} L_{i+1} d_{i+1} = \rho_i^{\text{out}} v_i^{\text{out}} L_i d_i + \rho_{i+1}^{\text{in}} v_{i+1}^{\text{in}} \bar{L}_{i+1} \Delta R, \quad (5)$$

where  $\bar{L}_{i+1} \equiv (L_i + L_{i+1})/2$ ,  $\rho_{i+1}^{\text{in}} \equiv \rho^{\text{in}}(\bar{R}_{i+1})$ , and  $v_{i+1}^{\text{in}} \equiv v^{\text{in}}(\bar{R}_{i+1})$  are the current sheet length, the ambient density, and the ambient velocity at  $R = \bar{R}_{i+1} \equiv R_i + \Delta R/2$ , respectively. The term on the left-hand side represents the mass flow through the upper surface  $L_{i+1} \times d_{i+1}$ , where  $L$  represents the length of the current sheet perpendicular to the plane of Fig. 8. The first term on the right-hand side represents the mass flow through the bottom surface  $L_i \times d_i$  and the second one the inflow across the SMS. The flow speeds  $v^{\text{out}}$  can be estimated as  $v_i^{\text{out}} = v_A(R_i) + v_{\text{sw}}(R_i)$  and  $v_{i+1}^{\text{out}} = v_A(R_{i+1}) + v_{\text{sw}}(R_{i+1})$ .

Bearing in mind the spherical geometry, the length  $L$  reads

$$L(R) = L(R_x) \frac{R}{R_x}, \quad (6)$$

where  $R_x$  is the radial distance of the diffusion region and  $L(R_x)$  is the current sheet extension in the  $\hat{\varphi}$ -direction at  $R_x$ , i.e., it represents the length of the current sheet X-line. The width of the current sheet at a given radial distance can be evaluated using

$$d_{i+1} = d_i \frac{R_{i+1}}{R_i} + \Delta R \phi_{i+1}, \quad (7)$$

with  $d_x \equiv d(R_x) \sim 0$ , i.e.,  $d_1 = \phi_1 \Delta R$ . The first term on the right-hand side of Eq. (7) is due to the spherical geometry (hereinafter we abbreviate  $d_i R_{i+1}/R_i \equiv d_{i+1}^*$ , i.e.,  $d_{i+1} =$

$d_{i+1}^* + \Delta R \phi_{i+1}$ ), and the second term is due to the inclination of the SMS with respect to the local radial direction (Fig. 8).

Equations (1–7) provide evaluation of the density distribution along the post CME-ray,  $\rho_{\text{out}}(R)$ , for various values of diffusion region height  $R_x$ . In Fig. 9 we show the results obtained using the coronal magnetic field model by Dulk & McLean (1978) and Mann et al. (1999b), whereas for the coronal density we use the isothermal ( $10^6$  K) solar wind model by Mann et al. (1999a).

Let us now consider the plasma temperature along the current sheet. In the first layer above the X-line the temperature equals the temperature  $T_{\text{SMS}}$  evaluated by Eq. (4) at the radial distance  $R = \bar{R}_1 \equiv R_x + \Delta R/2$ . The plasma of this temperature moves outward and enters into the next layer through the area  $d_1 \times L_1$ , undergoing adiabatic cooling due to volume expansion. In the second layer it meets with the plasma which inflows into the current sheet through the slow mode shock, where it was heated to  $T_{\text{SMS}}(\bar{R}_2)$ . The same happens successively in each further level.

Since thermal conductivity of coronal plasma is very high, the temperature can be consider as uniform across each layer, i.e., along the magnetic field lines connecting SMSs (magnetic field component  $B_\theta$ ). Thus, we can write for the temperature of a given layer:

$$T_{\text{CS}} = \frac{m_d T_d + m_{\text{SMS}} T_{\text{SMS}}}{m_d + m_{\text{SMS}}}. \quad (8)$$

Here,  $m_d$  and  $T_d$  are the mass and temperature of the plasma contained in the volume defined by the lines denoted in Fig. 8 as  $d_i$  and  $d_{i+1}^*$ . Note that we have neglected the thermal conductivity along the CS axis of symmetry, since the heat flow in this direction is reduced due to the magnetic field component  $B_\theta$ , and the temperature gradients are small due to large vertical length-scale of CS. The mass  $m_d$  is determined by:

$$m_d^{i+1} = \frac{\rho_{i+1} + \rho_i}{2} \Delta R \frac{L_{i+1} + L_i}{2} \frac{d_{i+1}^* + d_i}{2}, \quad (9)$$

whereas  $m_{\text{SMS}}$  and  $T_{\text{SMS}}$  are the mass and temperature of the plasma contained in the “triangular” volume between the radial and the slow mode shock. The temperature  $T_{\text{SMS}}$  can be evaluated by Eq. (4) at the radial distance  $R = \bar{R}_{i+1} \equiv R_i + \Delta R/2$ , whereas the mass  $m_{\text{SMS}}$  is determined by:

$$m_{\text{SMS}}^{i+1} = \rho_{\text{SMS}}^{i+1} \Delta R \frac{L_{i+1} + L_i}{2} \frac{\Delta R \phi_{i+1}}{2}. \quad (10)$$

where  $\rho_{\text{SMS}}^{i+1}$  is evaluated by Eq. (3) at the radial distance  $R = \bar{R}_{i+1} = R_i + \Delta R/2$ .

The estimate of the temperature  $T_{\text{CS}}$  in a given layer still requires evaluation of the temperature  $T_d$ , where we have to take into account the adiabatic expansion from the layer “ $i$ ” to “ $i+1$ ”. The plasma contained in the volume defined by lines  $d_{i-1}$  and  $d_i$ :

$$V_i = \Delta R \frac{L_i + L_{i-1}}{2} \frac{d_i + d_{i-1}}{2}, \quad (11)$$

expands into the volume:

$$V_{i+1} = \Delta R \frac{L_{i+1} + L_i}{2} \frac{d_{i+1}^* + d_i}{2} + (L_{i+1} d_{i+1}^* v_{i+1}^{\text{out}} - L_i d_i v_i^{\text{out}}) \Delta t. \quad (12)$$

The time  $\Delta t$  can be expressed as

$$\Delta t = \frac{\Delta R}{\bar{v}_{i+1}^{\text{out}}}, \quad (13)$$

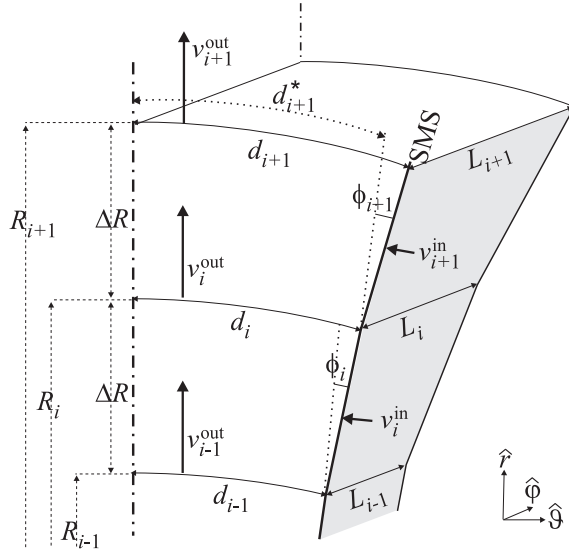


**Fig. 8.** Geometry of the post-CME ray model. Dash-dotted lines depict the axis of symmetry, shaded area represents the slow mode shock (SMS) and dotted lines the local radial direction. Local coordinate system is indicated in the lower-right corner. For details see the text in the Appendix.

where  $\bar{v}_{i+1}^{\text{out}} = (v_{i+1}^{\text{out}} + v_i^{\text{out}})/2$ . The difference of the first term on the right-hand-side of Eq. (12) and  $v_i$  represents the expansion in  $\hat{\phi}$  and  $\hat{\theta}$  direction, whereas the second term on the right-hand-side of Eq. (12) represents the contribution of the expansion in the  $\hat{r}$ -direction. Bearing in mind the characteristics of the adiabatic expansion, finally we get:

$$T_d^{i+1} = T_{\text{CS}}^i \left( \frac{V_i}{V_{i+1}} \right)^{(\gamma-1)}, \quad (14)$$

where  $\gamma$  is the ratio of specific heats, for hydrogen plasma being equal to  $\gamma = 5/3$ .

The system Eqs. (1–14) can be solved starting from the first layer above the diffusion region, and successively calculating the values in every new layer by using the values obtained for previous layer. In this way we get the dependencies  $\rho(R)$  and  $T(R)$  for the current sheet plasma.

*Acknowledgements.* We thank ISSI (International Space Science Institute, Bern) for the hospitality provided to the members of the team on the Role of Current Sheets in Solar Eruptive Events where many of the ideas presented in this work have been discussed. G.P. acknowledges support from ASI/INAF I/015/07/0.

## References

- Asai, A., Yokoyama, T., Shimojo, M., & Shibata, K. 2004, *ApJ*, 605, L77
- Aschwanden, M. J., Kosugi, T., Hudson, H. S., Wills, M. J., & Schwartz, R. A. 1996, *ApJ*, 470, 1198
- Aurass, H., Vršnak, B., & Mann, G. 2002, *A&A*, 384, 273
- Bárta, M., Vršnak, B., & Karlický, M. 2008, *A&A*, 477, 649
- Bemporad, A., Poletto, G., Landini, F., & Romoli, M. 2008, *Ann. Geophys.*, in press
- Bemporad, A., Poletto, G., Suess, S. T., et al. 2006, *ApJ*, 638, 1110
- Billings, D. E. 1966, *A guide to the solar corona* (New York: Academic Press, —c1966)
- Brueckner, G. E., Howard, R. A., Koomen, M. J., et al. 1995, *Sol. Phys.*, 162, 357
- Carmichael, H. 1964, in *The Physics of Solar Flares*, ed. W. N. Hess, 451
- Ciaravella, A. & Raymond, J. C. 2008, *ApJ*, in press

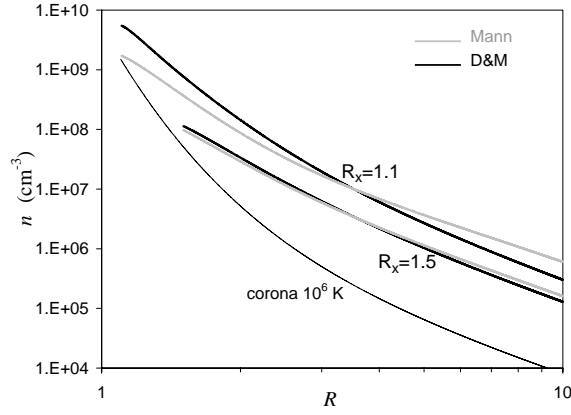


**Fig. 9.** Current sheet number-density calculated using the coronal magnetic field model by Dulk & McLean (1978) and Mann et al. (1999b); thick-black and thick-gray lines, respectively. The solar wind density model by Mann et al. (1999a) is drawn by thin-gray line (denoted as “corona  $10^6$  K”).

- Ciaravella, A., Raymond, J. C., Li, J., et al. 2002, *ApJ*, 575, 1116
- Dulk, G. A. & McLean, D. J. 1978, *Sol. Phys.*, 57, 279
- Forbes, T. G. & Acton, L. W. 1996, *ApJ*, 459, 330
- Furth, H. P., Killeen, J., & Rosenbluth, M. N. 1963, *Physics of Fluids*, 6, 459
- Gary, G. A. 2001, *Sol. Phys.*, 203, 71
- Gekelman, W. & Pfister, H. 1988, *Physics of Fluids*, 31, 2017
- Hirayama, T. 1974, *Sol. Phys.*, 34, 323
- Innes, D. E., McKenzie, D. E., & Wang, T. 2003, *Sol. Phys.*, 217, 247
- Innes, D. E., McKenzie, D. E., & Wang, T. 2003b, *Sol. Phys.*, 217, 267
- Ko, Y.-K., Raymond, J. C., Lin, J., et al. 2003, *ApJ*, 594, 1068
- Kohl, J. L., Esser, R., Gardner, L. D., et al. 1995, *Sol. Phys.*, 162, 313
- Kopp, R. A. & Pneuman, G. W. 1976, *Sol. Phys.*, 50, 85
- Lee, J.-Y., Raymond, J. C., Ko, Y.-K., & Kim, K.-S. 2006, *ApJ*, 651, 566
- Lin, J. 2004, *Sol. Phys.*, 219, 169
- Lin, J., Ko, Y.-K., Sui, L., et al. 2005, *ApJ*, 622, 1251
- Mann, G., Jansen, F., MacDowall, R. J., Kaiser, M. L., & Stone, R. G. 1999a, *A&A*, 348, 614
- Mann, G., Klassen, A., Estel, C., & Thompson, B. J. 1999b, in *ESA Special Publication*, Vol. 446, 8th SOHO Workshop: Plasma Dynamics and Diagnostics in the Solar Transition Region and Corona, ed. J.-C. Vial & B. Kaldeich-Schü, 477
- Marić, D., Vršnak, B., Stanger, A. L., et al. 2007, *Sol. Phys.*, 241, 99
- Masuda, S., Kosugi, T., Hara, H., Tsuneta, S., & Ogawara, Y. 1994, *Nature*, 371, 495
- McKenzie, D. E. & Hudson, H. S. 1999, *ApJ*, 519, L93
- Parker, E. N. 1958, *ApJ*, 128, 664
- Petschek, H. E. 1964, in *The Physics of Solar Flares*, ed. W. N. Hess, 425
- Poland, A. I., Howard, R. A., Koomen, M. J., Michels, D. J., & Sheeley, Jr., N. R. 1981, *Sol. Phys.*, 69, 169
- Poletto, G., Bemporad, A., Landini, F., & Romoli, M. 2008, *Ann. Geophys.*, in press
- Raymond, J. C., Ciaravella, A., Dobrzycka, D., et al. 2003, *ApJ*, 597, 1106
- Riley, P., Linker, J. A., Mikić, Z., et al. 2002, *ApJ*, 578, 972
- Riley, P., Lionello, R., Mikić, Z., et al. 2007, *ApJ*, 655, 591
- Roussev, I. I., Forbes, T. G., Gombosi, T. I., et al. 2003, *ApJ*, 588, L45
- Saez, F., Llebaria, A., Lamy, P., & Vibert, D. 2007, *A&A*, 473, 265
- Sheeley, Jr., N. R. & Wang, Y.-M. 2002, *ApJ*, 579, 874
- Sheeley, Jr., N. R. & Wang, Y.-M. 2007, *ApJ*, 655, 1142

- Sheeley, Jr., N. R., Warren, H. P., & Wang, Y.-M. 2004, *ApJ*, 616, 1224
- Simnett, G. M., Tappin, S. J., Plunkett, S. P., et al. 1997, *Sol. Phys.*, 175, 685
- Skender, M., Vršnak, B., & Martinis, M. 2003, *Phys. Rev. E*, 68, 046405
- Soward, A. M. & Priest, E. R. 1982, *Journal of Plasma Physics*, 28, 335
- Sturrock, P. A. 1966, *Nature*, 211, 695
- Sui, L., Holman, G. D., & Dennis, B. R. 2004, *ApJ*, 612, 546
- Sui, L., Holman, G. D., White, S. M., & Zhang, J. 2005, *ApJ*, 633, 1175
- Švestka, Z. F., Fontenla, J. M., Machado, M. E., Martin, S. F., & Neidig, D. F. 1987, *Sol. Phys.*, 108, 237
- Török, T., Kliem, B., & Titov, V. S. 2004, *A&A*, 413, L27
- Tsuneta, S. 1996, *ApJ*, 456, 840
- Tsuneta, S., Hara, H., Shimizu, T., et al. 1992, *PASJ*, 44, L63
- Ugai, M. 1987, *Geophys. Res. Lett.*, 14, 103
- Veronig, A. M., Karlický, M., Vršnak, B., et al. 2006, *A&A*, 446, 675
- Vourlidas, A., Buzasi, D., Howard, R. A., & Esfandiari, E. 2002, in *ESA Special Publication*, Vol. 506, *Solar Variability: From Core to Outer Frontiers*, ed. J. Kuijpers, 91–94
- Vourlidas, A., Subramanian, P., Dere, K. P., & Howard, R. A. 2000, *ApJ*, 534, 456
- Vršnak, B. 2008, *Annales Geophysicae*, 26, 3089
- Vršnak, B., Magdalenic, J., Aurass, H., & Mann, G. 2002, *A&A*, 396, 673
- Vršnak, B., Magdalenic, J., & Zlobec, P. 2004, *A&A*, 413, 753
- Vršnak, B. & Skender, M. 2005, *Sol. Phys.*, 226, 97
- Vršnak, B., Temmer, M., Veronig, A., Karlický, M., & Lin, J. 2006, *Sol. Phys.*, 234, 273
- Vršnak, B., Klein, K.-L., Warmuth, A., Otruba, W., & Skender, M. 2003, *Sol. Phys.*, 214, 325
- Wang, Y.-M., Sheeley, N. R., Howard, R. A., St. Cyr, O. C., & Simnett, G. M. 1999, *Geophys. Res. Lett.*, 26, 1203
- Webb, D. F., Burkepile, J., Forbes, T. G., & Riley, P. 2003, *Journal of Geophysical Research (Space Physics)*, 108, 1440
- Webb, D. F. & Cliver, E. W. 1995, *J. Geophys. Res.*, 100, 5853
- Yokoyama, T., Akita, K., Morimoto, T., Inoue, K., & Newmark, J. 2001, *ApJ*, 546, L69